Contrib Mineral Petrol (1992) 112:329–340

Contributions to Mineralogy and Petrology


# Highly reducing conditions during Alpine metamorphism of the Malenco peridotite (Sondrio, northern Italy) indicated by mineral paragenesis and $H_2$ in fluid inclusions

**Adolf Peretti[1] *, Jean Dubessy[2], Josef Mullis[3], B. Ronald Frost[4], and V. Trommsdorff[5]**

[1] Institut für Mineralogie und Petrographie, ETH, Sonneggstrasse 5, CH-8092 Zurich, Switzerland
[2] CREGU, GS CNRS 077, BP 23, F-54501 Vandoeuvre-Les-Nancy Cedex, France
[3] Mineralogisch Petrographisches Institut der Universität, Bernoullistrasse 30, CH-4056 Basel, Switzerland
[4] Department of Geology and Geophysics, University of Wyoming, Laramie, WY 82071, USA
[5] Institut für Mineralogie und Petrographie, ETH, Sonneggstrasse 5, CH-8092 Zurich, Switzerland

Received April 12, 1991 / Accepted June 19, 1992

**Abstract.** During regional metamorphism of the Malenco serpentinized peridotite (Sondrio, northern Italy), the mineral assemblage pentlandite-awaruite-magnetite-native copper-antigorite-brucite-olivine-diopside is formed. The opaque assemblage indicates very reduced fluids with $fO_2$ values 4 log units below QFM. Primary fluid inclusions were trapped in diopside overgrowth, contemporaneous with the opaque assemblage. These metamorphic fluids are saline aqueous solutions (about 10.4 mol% NaCl equivalent) and contain molecular $H_2$ of approximately 1 mol%, as shown by micro-Raman analysis and microthermometry. The fluids are interpreted to have been formed during deserpentinization at the olivine-in isograd under strong reducing conditions.

## Introduction

$H_2$ is a common fluid species in many present-day geothermal fluids (e.g. Ellis 1979; Arnorsson 1985). However, $H_2$ is almost never found in fluid inclusions for three main reasons. First, upon cooling after trapping, partial chemical reequilibration in the system C–O–H–(N–S) produces very low $H_2$ concentrations. In such systems $H_2$ is not detectable by micro-Raman analysis inside individual inclusions (Dubessy 1984; Dubessy et al. 1989). Second, the redox state of initial fluids is usually too high to stabilize detectable high $H_2$ concentrations. Third, $H_2$ is a possible candidate to diffuse as shown by Hollister and Burruss (1976), Hall and Bodnar (1990) and Hall et al. (1990).

It has long been known that serpentinization of ultramafic rocks may reduce incoming fluids (Thayer 1966; Barnes and O'Neil 1969). Petrographic study of the metamorphosed Malenco peridotite in the Alps (De Quervain 1963; Evans and Trommsdorff 1970; Peretti 1988) has evidenced mineral parageneses (formation of awaruite) indicative of highly reducing conditions during the prograde alpine metamorphism. The aim of this study is to obtain information about the prograde metamorphic fluids at the site of dehydration reactions of serpentinite (olivine-in isograd) and the contemperaneous formation of awaruite.

* *Present address:* Kehlhofweg 4, 6043 Adligenswil, Switzerland

*Correspondence to:* A. Peretti

## Geological setting

The Malenco serpentinite is part of a ophiolite suture zone in the eastern part of the Central Alps (Dietrich 1969; Ferrario and Montrasio 1976; De Capitani et al. 1981; Peretti 1985). The Malenco ophiolites are mainly composed of ultramafitites. In analogy to ophiolites in the northern part of the suture zone (P, L and F, Fig. 1), the Malenco serpentinites are interpreted as Mesozoic in age.

Tectonically, the Malenco serpentinite represents a huge ultramafic nappe (Fig. 1) covering an area of 200 km$^2$ with a thickness of about 2 km (Staub 1946). It is situated between the Margna and the Suretta nappes which have a pre-Mesozoic basement and a Mesozoic cover. The Suretta nappe with its equivalent in the Lanzada-Scermendone zone (L–S, Fig. 1) can be found as a tectonic window within the Malenco nappe (Staub 1946; Montrasio 1984). The overlying Margna nappe completely surrounds the Malenco nappe, reflecting later tectonic events that folded both the Margna and the Malenco nappe into a broad anticlinal structure. The nappes have been intruded after their formation by the younger Bregaglia intrusives (gabbro, tonalite, granodiorite). The tectonic and metamorphic history of the Malenco serpentinite is polyphase and shows many similarities with those found in the Margna nappe (Liniger and Guntli 1988).

### *Tectonic history of the Malenco serpentinite*

The complex metamorphic and tectonic history of the Malenco nappe is analyzed by the study of field relations as shown in Fig. 2 and listed next. The three main phases of deformation have been mentioned by Bucher and Pfeifer (1973).

f0. *A small-scale layering (So) is outlined by concentrations of spinel and pyroxene which are cut by basic dykes. Rodingitization of dykes occurs before subsequent folding.*

f1. *(So)-layering and rondingite (Ro) are folded isoclinally. The*

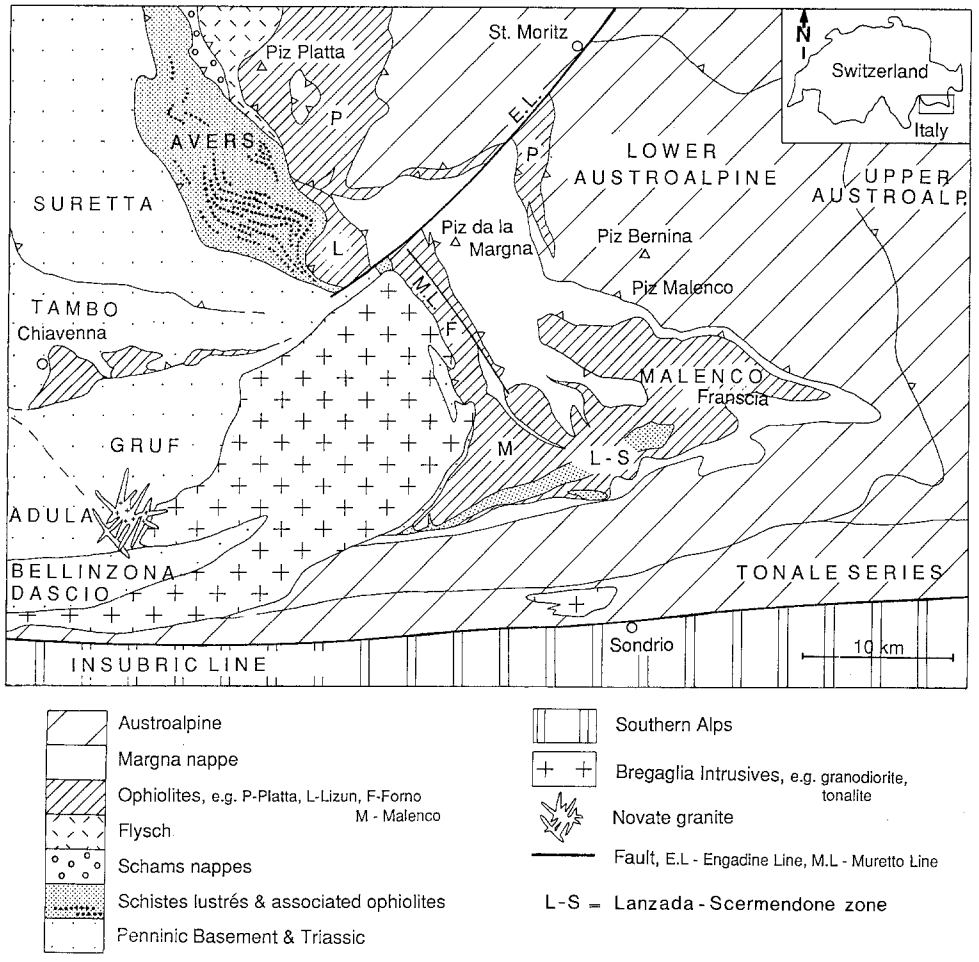


**Fig. 1.** Geological and tectonic map of the contact zone between the Central Alps and the lower Austro-Alpine nappe showing an ophiolite suture zone including the Malenco nappe (modified from Trommsdorff and Nievergelt 1983)

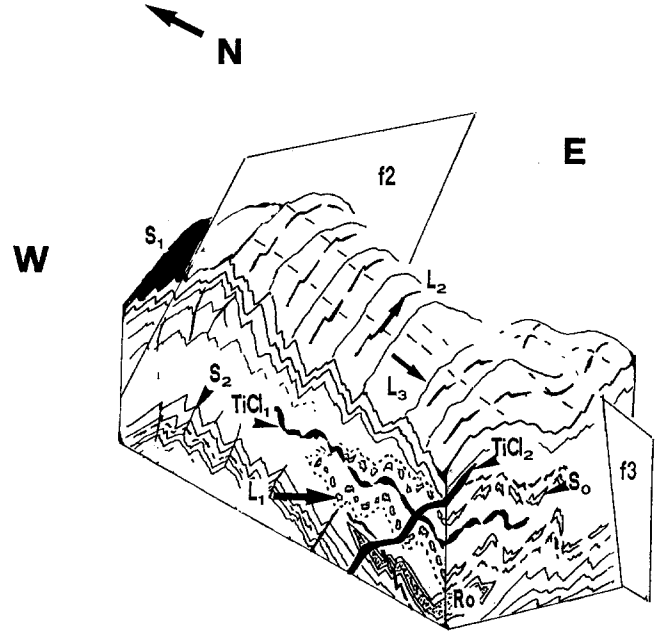


**Fig. 2.** Schematic 3D diagram showing the field relations at the site of fluid inclusion occurrences in metaserpentinite. Structures related to three main deformation phases (f1, f2 and f3) as discussed in the text. *So*, layering; $S_{1,2}$, schistosity; $L_{1,2,3}$, lineation; *Ro*, rondingite; $TiCl_{1,2}$. Titanian clinohumite veins

*extension lineation $L_1$ (NW–SE direction) is formed by elongation of spinel and pyroxene which are pseudomorphosed at the same time by fine grained metamorphic minerals in mylonites. The dominant schistosity ($S_1$) develops.*

f2. *A harmonic, open and asymetric folding style occurs with formation of the second schistosity ($S_2$) and crenulation lineation $L_2$.*

f3. *A third folding event comparable to f2 establishes other orientations and is less dominant.*

Several generations of titanian clinohumite-olivine veins can be distinguished as shown in Fig. 2. Early veins ($TiCl_1$) cross the layering of the ultramafitite as well as the metasomatic zonation accompanying the rondingite. They are strongly boudinaged and folded during f2. The second generation ($TiCl_2$) is focused in shear zones that postdate f2. The structures are interpreted next in chronological sequence:

1. Pre-metamorphic magmatic processes represented by cumulative layering (So) and occurrence of basic dykes.
2. Rodingitization of basic dykes before folding indicating pre-Alpine-metamorphic sea-floor serpentinization of peridotite.
3. Alpine deformation phases with emplacement of nappes (f1) followed by backfolding (f2, f3). F2 causes large E–W trending anti- and synform structures of the Malenco nappe.

As can be seen from different generations of metamorphic minerals, metamorphism of serpentinites at greenschist facies conditions occurred during f1, f2 as well as during a postkinematic metamorphic annealing (Mellini et al. 1987). Unlike Bucher and Pfeifer (1973), the age of antigorite schistosity is interpreted as Alpine $S_1$ and the f2 structures are correlated with large anti- and synform structures rather than the f3 phase. The titanian-clinohumite-olivine veins are interpreted as fluid-channeling shear zones that were

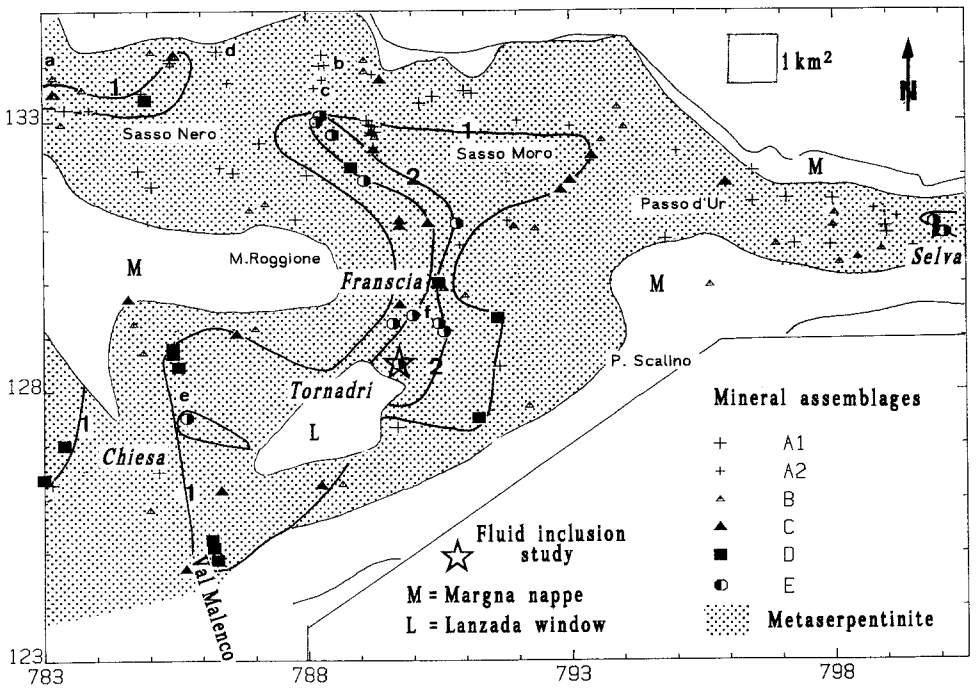


**Fig. 3.** Mapping of metamorphic mineral assemblages (Peretti 1988). 1. olivine-in with the absence of brucite; 2. olivine-in with the presence of brucite. The *open star* indicates the locality of fluid inclusion study (assemblages *A* to *E*, see Table 1)

**Table 1.** Change in silicate assemblages (system CaO–MgO–SiO2–H2O) in the Malenco serpentinite with increasing grade of regional metamorphism from A to E (mapping see Fig. 3). Note change in grain size habit of antigorite. Chrysotile abundance based on Mellini et al. (1987)

| Phase assemblage | chry | anA | anB | anC | bru | olA | olB | dioA | dioB |
|---|---|---|---|---|---|---|---|---|---|
| A1, A2 | X | X | | | | | | X | X |
| B | X | X | X | | | (X) | | X | X |
| C | X | | X | X | | X | | X | X |
| D | X | | X | X | | X | X | X | X |
| E | (X) | | | X | (X) | X | X | (X) | X |

chry, Submicroscopic chrysolite; anA, fine grained xenomorphic antigorite; anB, fine grained idiomorphic antigorite; anC, coarse grained idiomorphic antigorite; bru, brucite; olA, olivine veins (different generations); olB, new olivine (mosaic with antigorite C); dioA, recrystallized old diopside; dioB, mosaic or epitaxial new diopside

active in conjunction with the main regional metamorphic events in the Malenco serpentinite in coincidence with the interpretation of Trommsdorff and Evans (1980).

## Regional metamorphism and mineral reactions

The interference of the metamorphism with the tectonic events caused a complex isograd pattern (Figs. 3 and 5). The studied area does not exhibit any contact metamorphism as it is the case in the western part of the Malenco nappe (Evans and Trommsdorff 1970). The regional metamorphism is defined by mineral assemblages that represent a prograde sequence ranging from the upper stability limits of chrysotile to the lower limits of the olivine facies. Detailed mapping of the metamorphic silicates and hydroxides shows the occurrence of olivine in two different assemblages (Fig. 3, Table 1): (1) olivine-antigorite ± chrysotile, (2) antigorite-brucite-olivine. The dehydration equilibria (a) and (b) were formulated on the basis of these observed phases (Table 2). In the system $MgO-SiO_2-H_2O$ equilibrium (a) is metastable whereas equilibrium (b) is a stable P–T univariant dehydration reaction (Evans

**Table 2.** P-T univariant dehydration reactions (a–c) and $f(O_2)-f(S_2)$ univariant opaque equilibria (d–f) for given pentlandite composition

Equilibria involving silicates

(a) $20\ Mg_3Si_2O_5(OH)_4 = Mg_{48}Si_{34}O_{85}(OH)_{62} + 6\ Mg_2SiO_4 + 9\ H_2O$
chrysotile — antigorite — olivine

(b) $Mg_{48}Si_{34}O_{85}(OH)_{62} + 20\ Mg(OH)_2 = 34\ Mg_2SiO_4 + 51\ H_2O$
antigorite — brucite — olivine

(c) $8\ CaMgSi_2O_6 + Mg_{48}Si_{34}(OH)_{62} = 18\ Mg_2SiO_4 + 4\ Ca_2Mg_5Si_8O_{22}(OH)_2 + 27\ H_2O$
diopside — antigorite — olivine — tremolite

Equilibria involving opaque phases

(d) $0.759\ Fe_{4.96}Ni_{3.95}S_8 + 2.510\ O_2 = 0.5\ Ni_3S_2 + 1.255\ Fe_3O_4 + 2.038\ S_2$
pentlandite — heazlewoodite — magnetite

(e) $0.759\ Fe_{4.96}Ni_{3.95}S_8 + 1.843\ O_2 = FeNi_3 + 0.921\ Fe_3O_4 + 1.5\ S_2$
pentlandite — awaruite — magnetite

(f) $Ni_3S_2 + 0.333\ Fe_3O_4 = FeNi_3 + 0.666\ O_2 + S_2$
heazlewoodite — magnetite — awaruite

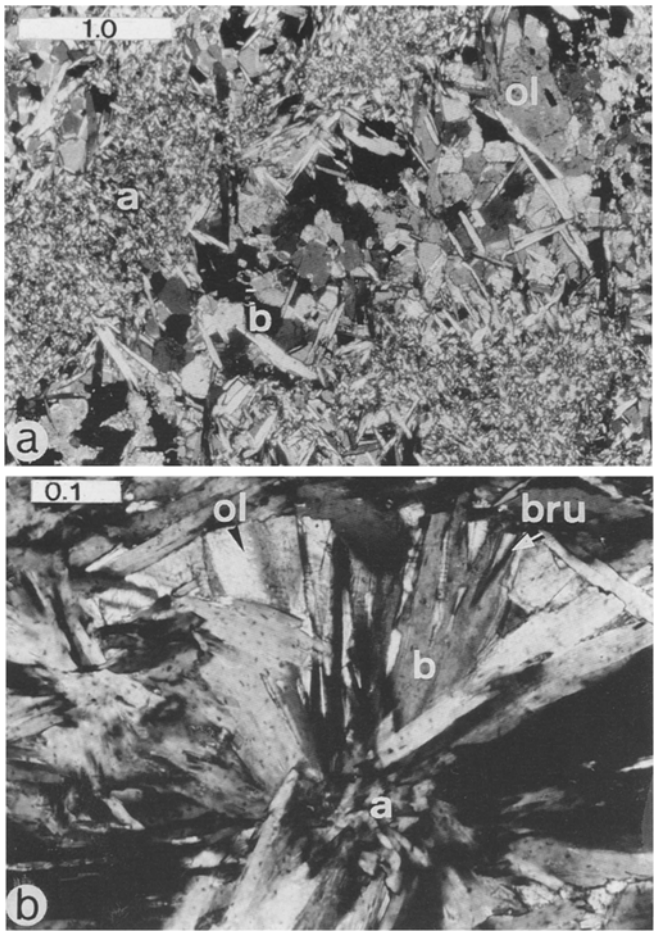


**Fig. 4a, b.** Mineral paragenesis at the olivine-in (microphotographs in polarized light). **a** Microphotograph of antigorite-olivine schist. Note the increase of grain size and the idiomorphic habit of antigorite associated to olivine (Swiss coordinates: 783380/127000). **b** Microphotograph of brucite-olivine-antigorite schist. Brucite is interlayered with antigorite (Swiss coordinates: 790825/130725). *a*, Fine grained xenomorphic antigorite; *b*, coarse grained idiomorphic antigorite; *ol*, olivine; *bru*, brucite. The bar scale is in mm units

et al. 1976). Because of the submicroscopic occurrence of chrysotile (Mellini et al. 1987), the formation of olivine from chrysotile has still to be documented by HR-TEM analyses. In contrast, the growth of olivine from antigorite and brucite can be shown microscopically (Fig. 4). The increase in metamorphic grade is documented by an increase in grain size and by the crystal habit of antigorite (Table 1, Fig. 4) as described by Mellini et al. (1987). Diopside is a stable mineral during regional metamorphism. Its stability is limited with increasing metamorphic grade (Evans and Trommsdorff 1970) during the Bregaglia contact metamorphism in the western part of the Malenco serpentinite [reaction (c), Table 2].

Detailed mapping of opaque assemblages (Peretti 1988) has shown that three main regional metamorphic assemblages occur in the Malenco serpentinite (separated by lines 1 and 2, Fig. 5). The assemblages pentlandite-heazlewoodite-magnetite, pentlandite-awaruite-magnetite and finally heazlewoodite-awaruite-magnetite occur successively with increasing metamorphic grade. Each assemblage (Fig. 6) constrains the $f(O)_2/f(S_2)$-ratio for given pressure and temperature (Eckstrand 1975) (Table 2). A schematic log $f/(S_2) - \log f(O_2)$ phase diagram of the $Fe-Ni-O_2-S_2$ system is given in Fig. 7. At given P and T, the most reducing assemblage is pentlandite-awaruite-magnetite. The highly reducing conditions are confirmed by the occurrence of native copper in samples containing pentlandite-awaruite-magnetite and heazlewoodite-awaruite-magnetite. The awaruite-in isograd in the Malenco serpentinite coincides approximately with the olivine-in isograd (Figs. 3, 5).

## Petrography of rock samples containing fluid inclusions

The studied samples containing the fluid inclusions originate from a quarry close to Tornadri (Swiss coordinates 789725/128500). The outcrop is situated at the isograd antigorite + brucite → olivine + fluid and within the stability field of pentlandite, awaruite and magnetite, just at the disappearence of pentlandite and the appearance of heazlewoodite-awaruite-magnetite (Figs. 3, 5).

### *Microscopic observations*

The studied fluid inclusions are associated with alpine metamorphic minerals as shown in Figs. 8 and 9. Several generations of metamorphic minerals can be distinguished. Both olivine and diopside occur as two generations, denoted A and B. A first generation

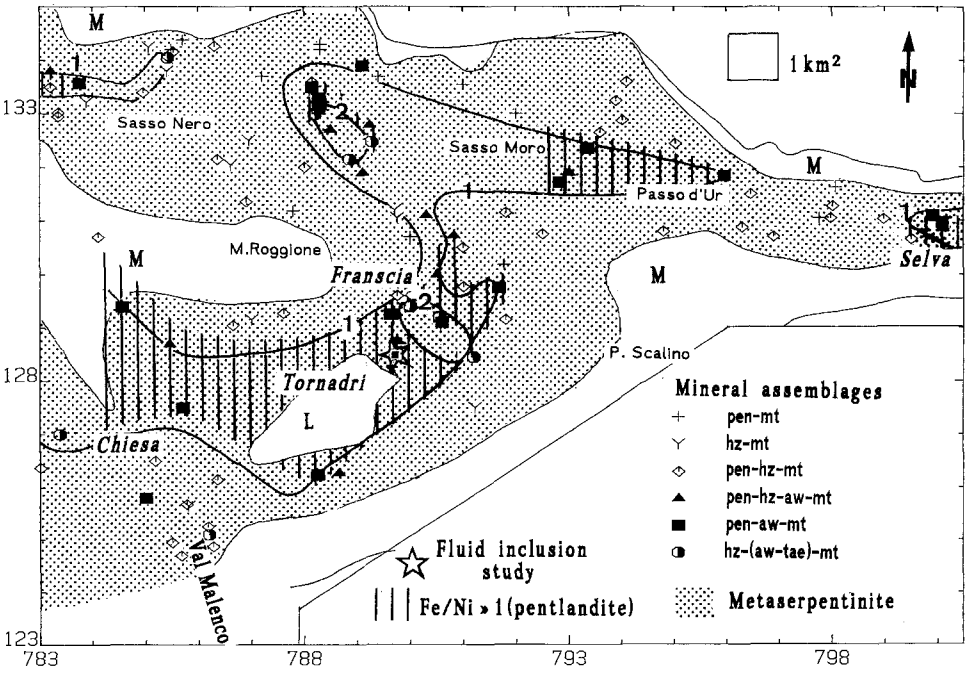


**Fig. 5.** Map of opaque minerals with prograde metamorphism (Peretti 1988). *1*, Appearance of awaruite in the presence of pentlandite showing most reducing conditions. *2*, Disappearance of pentlandite indicating relative oxidation with respect to 1. *pen*, pentlandite; *hz*, heazlewoodite; *aw*, awaruite; *tae*, taenite; *mt*, magnetite. The *shaded area* denotes occurrence of pentlandite with Fe/Ni ratio >1. The *open star* indicates the locality of fluid inclusion study

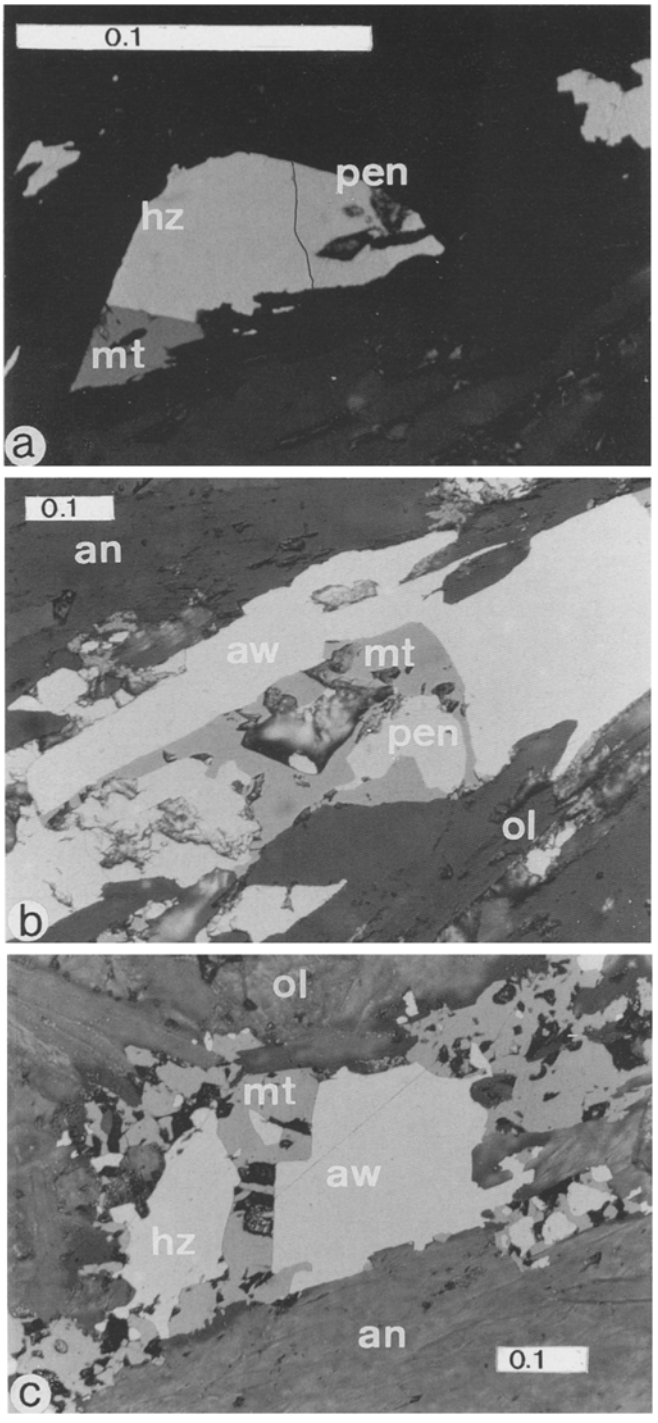


**Fig. 6a–c.** Metamorphic opaque assemblages (microphotographs in reflected light and with parallel nicols). **a** Assemblage pen-hz-mt occurring in a chlorite-diopside-antigorite schist (Swiss coordinates: 791800/131150); **b** assemblage pen-aw-mt occurring in a brucite-diopside-olivine-antigorite schist (Swiss coordinates: 800000/130900); **c** assemblage hz-aw-mt occurring in a brucite-olivine-antigorite schist (Mg 159c; Swiss coordinates: 790000/129400). *pen*, pentlandite; *ol*, olivine; *an*, antigorite. Scale in mm units

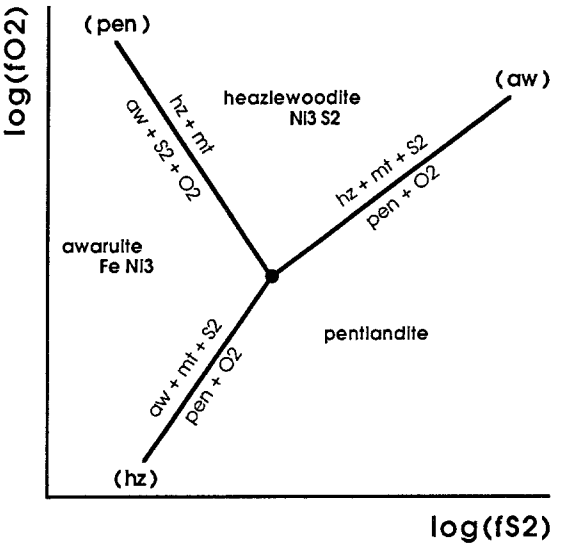


**Fig. 7.** Projection of the stability fields of pentlandite, awaruite and heazlewoodite (magnetite always present) in the $\log fO_2 - \log fS_2$ plane. Chemical composition of pentlandite: $Fe_{4.96}Ni_{3.95}S_8$. (*aw*), pentlandite-heazlewoodite-magnetite assemblage; (*hz*), pentlandite-awaruite-magnetite assemblage; (*pen*), heazlewoodite-awaruite-magnetite assemblage. *aw*, awaruite; *pen*, pentlandite; *hz*, heazlewoodite; *mt*, magnetite

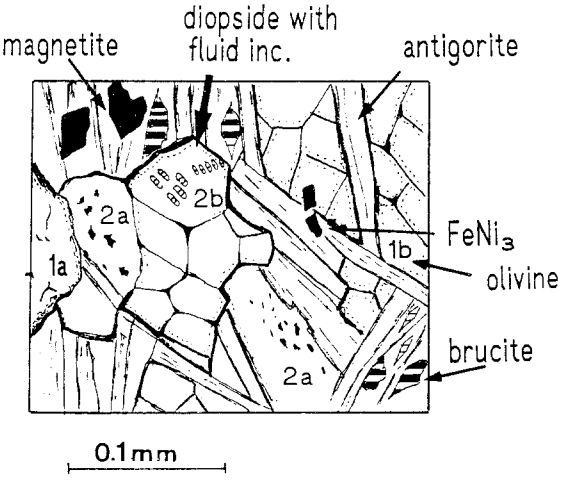


**Fig. 8.** Texture of metamorphic minerals in a section parallel to schistosity ($S_1$). Fluid inclusions in this section occur as early secondary in recrystallized mosaic diopside (L2 inclusions). 1*a*, old olivine; 1*b*, new recrystallized olivine; 2*a*, old diopside containing opaques; 2*b*, new recrystallized diopside

of olivine is relatively large and shows irregular fractures (Fig. 8, 1a). The second generation is recrystallized olivine A which is typically intergrown between large idiomorphic antigorite blades (Fig. 8, 1b). Diopside A occurs as large crystals with abundant opaque inclusions, mainly magnetite, replacing original pyroxenes (Fig. 8, 2a). Diopside B shows recrystallized mosaic-like textures (Fig. 8) or occurs as epitaxial overgrowths on early relict diopside A (Fig. 9). Brucite is localized between the antigorite blades and in a texture that indicates that it is part of the stable mineral assemblage and not a late alteration product of olivine. Antigorite is the typical coarse grained and idiomorphic type described by Mellini et al. (1987) for their sample Mg159. Pentlandite, awaruite ($FeNi_3$) and magnetite are adjacent to diopside B or are solid inclusions in the epitaxial diopside. Native copper is found in addition to chalcocite, millimeter-size awaruite and magnetite crystals. Graphite was not identified in spite of the numerous analytical methods used: reflected light microscopy, scanning electron microscopy, dissolution of the rock in HF plus aquae regiae, and DGTA analysis.

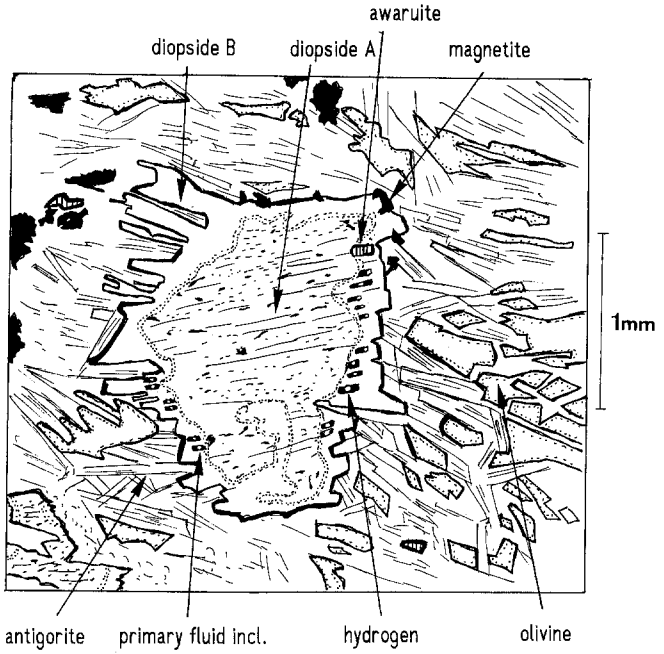


**Fig. 9.** Epitaxial growth of diopside B around old prekinematic diopside A. Primary fluid inclusions containing hydrogen are situated at the beginning of expitaxial diopside B overgrowth. Awaruite and magnetite are formed next to fluid inclusions. The nonopaque assemblage is olivine-antigorite-diopside-brucite. The analyzed fluid inclusion containing hydrogen is indicated

### *Chemical composition and structural characterization of solid phases*

The chemical compositions of the minerals were determined with electron microprobe analyses (Table 3a–c) using an automated ARL SEMQ microprobe operated at an acceleration potential of 15 kV (20 nA sample current). Reference standards were natural and synthetic silicates, oxides and sulfides. Because of the complex structure of antigorite its formula is written as $Mg_{3m-3}\ Si_{2m}\ O_{5m}\ (OH)_{4m-6}$ (Kunze 1961). The antigorite of sample Mg 159 (Table 3a) was determined by HR-TEM analyses (Mellini et al. 1987) as ordered antigorite with $m=17$. As the locality of the fluid inclusion study is close to locality Mg 159, the same crystal structure was assumed for antigorite To3 (Table 3a). The $Fe^{3+}$ concentration was determined in sample Mg 159c by Mössbauer spectroscopy (Peretti 1988) and assumed to be similar in sample To3. The two generations of diopside differ chemically as described by Peters (1968). Diopside A (brownish color in plane polarized light) contains variable contents of $Na_2O$ ($\leq 0.4$ wt.%), $Al_2O_3$ ($\leq 0.8$ wt.%), $Cr_2O_3$ ($\leq 0.7$ wt.%) and MnO ($\leq 0.1$ wt.%). In contrast, the new diopside B, does not contain these impurities (Table 3b). Brucite contains $Cl^-$ above the microprobe detection limit, whereas the $Cl^-$ in antigorite is at the detection limit. Fluorine was detected in some samples of brucite (Table 3a). The $X_{Mg}$ of antigorite, olivine and brucite (Table 3a) represent typical values found in metamorphosed ultramafic rocks (Evans and Trommsdorff 1972; Trommsdorff and Evans 1974). This is an indication that the phases are in metamorphic equilibrium. The chemical composition of awaruite is nearly stoichiometric $FeNi_3$ (Table 3c). The crystal structure of awaruite was determined with a Gandolfi camera (FeK$\alpha$-radiation). The spacings $d_{111}=2.059$, $d_{200}=1.780$, $d_{220}=1.253$, $d_{311}=$

**Table 3a.** Chemical composition of minerals (in wt.%) found in serpentinites at the highest grade of regional metamorphism in the eastern Malenco nappe (greenschist facies)

| Mineral | Antigorite C | | Olivine B | | Brucite | | |
|---|---|---|---|---|---|---|---|
| Sample no. | Mg 159c | To3 | To3 | Mg 159c | To3 | | Mg 159c |
| $SiO_2$ | 43.32 | 41.81 | 41.13 | 40.98 | 0.00 | 0.00 | 0.00 |
| MgO | 39.62 | 39.10 | 50.36 | 49.56 | 61.81 | 62.49 | 63.69 |
| $Al_2O_3$ | 1.30 | 2.72 | – | – | – | – | – |
| $Cr_2O_3$ | 0.23 | 0.48 | 0.00 | 0.00 | – | – | – |
| NiO | 0.80 | 0.08 | 0.39 | 0.39 | – | – | – |
| MnO | 0.40 | 0.00 | 0.24 | 0.17 | 0.00 | 0.00 | 0.00 |
| FeO | 3.04 | 3.10 | 8.68 | 8.87 | 8.06 | 7.51 | 6.83 |
| F | 0.10 | – | – | – | <0.1 | 0.24 | <0.10 |
| Cl | 0.01 | <0.01 | – | – | 0.02 | 0.03 | 0.02 |
| | 87.62 | 87.29 | 100.80 | 99.99 | 69.89 | 70.27 | 70.54 |
| Normalized on the basis of | | | | | | | |
| O | 85 | 85 | 4 | 4 | | | |
| OH | 62 | 62 | | | 2 | 2 | 2 |
| $Fe^{3+}/Fe(tot)$ | 0.147[a] | 0.15 | – | – | – | – | – |
| Si | 33.254 | 32.280 | 0.996 | 1.001 | 0.000 | 0.000 | 0.000 |
| Al(IV) | 0.765 | 1.717 | – | – | – | – | – |
| Al(VI) | 0.408 | 0.765 | – | – | – | – | – |
| Mg | 45.348 | 45.016 | 1.819 | 1.805 | 0.932 | 0.937 | 0.943 |
| Cr | 0.136 | 0.289 | 0.000 | 0.000 | – | – | – |
| Ni | 0.051 | 0.003 | 0.008 | 0.008 | – | – | – |
| Mn | 0.017 | 0.000 | 0.005 | 0.004 | 0.000 | 0.000 | 0.000 |
| $Fe^{2+}$ | 1.161 | 1.700 | 0.176 | 0.181 | 0.068 | 0.063 | 0.057 |
| $Fe^{3+}$ | 0.289 | 0.306 | – | – | – | – | – |
| $X_{Mg}$ | 0.966 | 0.964 | 0.912 | 0.909 | 0.932 | 0.937 | 0.943 |

[a] Determined by Mössbauer spectroscopy (Peretti 1988)

1.070, $d_{222}=1.025$ and superlattice reflections at d=2.269, 1.390, 1.18, 1.135 were found as described for ordered awaruite by Leech and Sykes (1939), but also additional reflections were found. Heazlewoodite is stoichiometric $Ni_3S_2$ (optically anisotropic) and magnetite is almost pure $Fe_3O_4$ (Table 3b and c). The native copper contains small concentrations of Ni and Fe and the chalcocite is slightly nonstoichiometric $Cu_{1.9}$ $Fe_{0.07}S$ (Table 3c, locality SP). Pentlandite is Co-poor with a high metal/sulfur-ratio and a high Fe/Ni-ratio (Fe/Ni>1) as is typically found in the high grade regional metamorphic part of the Malenco serpentinite (Fig. 5). Cu-rich and Co-rich pentlandite occur only as relicts inside Co-poor pentlandite and awaruite.

**Table 3b.** Chemical composition of diopside and magnetite in regional metamorphosed serpentinite (in wt.%)

| Mineral | Diopside A | Diopside B | Magnetite | | |
|---|---|---|---|---|---|
| Sample no. | SP | SP | Sample no. | To3 | Mg 159c |
| $SiO_2$ | 52.86 | 54.54 | $TiO_2$ | 0.16 | 0.0 |
| MgO | 19.40 | 17.70 | $Al_2O_3$ | 0.01 | 0.08 |
| $Al_2O_3$ | 1.04 | 0.00 | $V_2O_3$ | – | 0.06 |
| $Cr_2O_3$ | 0.49 | 0.00 | $Cr_2O_3$ | 2.52 | 0.02 |
| NiO | 0.00 | 0.00 | $Fe_2O_3$[a] | 65.42 | 67.75 |
| MnO | 0.12 | 0.08 | FeO | 29.55 | 30.38 |
| FeO | 1.80 | 1.22 | MnO | 0.16 | 0.04 |
| CaO | 23.18 | 25.79 | MgO | 0.67 | 0.12 |
| $Na_2O$ | 0.30 | 0.05 | ZnO | 0.00 | 0.16 |
| | | | NiO | 0.43 | – |
| | 99.21 | 99.37 | | 98.92 | 98.61 |
| Normalized on the basis of 3 oxygens | | | | | |
| Si | 0.979 | 0.996 | Ti | 0.00 | 0.00 |
| Mg | 0.530 | 0.482 | Al | 0.00 | 0.00 |
| Al | 0.022 | 0.000 | Cr | 0.08 | 0.00 |
| Cr | 0.008 | 0.000 | $Fe^{3+}$[a] | 1.91 | 1.99 |
| Ni | 0.000 | 0.000 | $Fe^{2+}$ | 0.96 | 0.99 |
| Mn | 0.003 | 0.001 | Mn | 0.01 | 0.00 |
| $Fe^{2+}$ | 0.028 | 0.019 | Mg | 0.04 | 0.01 |
| Ca | 0.455 | 0.505 | Ni | 0.04 | – |
| Na | 0.029 | 0.002 | | | |
| $X_{Mg}$ | 0.956 | 0.963 | | | |

[a] Calculated on the basis of 4 oxygens and 3 cations

## Fluid inclusions

### *Fluid inclusion typology*

Fluid inclusions were studied in three different thin sections; in many other sections the fluid inclusions were too small for analysis. All inclusions occur in metamorphic diopside B (Fig. 10a, b). The maximum size of the inclusions never exceeds 10 µm. The size of the inclusions studied was usually between 5 and 8 µm. The inclusions are regular shaped tubes oriented along the (001) axis. At room temperature, they contain liquid and vapor phases with similar volume proportions (vapor=10–15 vol.%). A few of the inclusions contain a transparent mineral which does not dissolve upon heating experiments to 260° C, suggesting that it is a silicate.

Two populations of fluid inclusions were identified. Type L1 inclusions are found in the contact zone between the early colored diopside A and the epitaxially grown diopside B (Figs. 9, 10a). No fluid inclusion trails crosscut the boundary between the two pyroxenes. These textures show that fluid inclusions L1 are primary and were trapped at the initial growth of the epitaxial diopside B, just on the surface of diopside A. Type L2 inclusions are situated along healed fractures in diopside B crystals (Figs. 8, 10b). The trails containing the analyzed fluid inclusions within diopside do not crosscut the grain boundaries between adjacent diopside crystals.

### *Microthermometry*

Fluid inclusions were measured with a Chaixmeca stage (Poty et al. 1976). Temperatures of the following phase transitions were measured if the size of the inclusion was large enough for unambiguous observations: the first melting, which is the eutectic of the electrolyte solution (Te), the dissociation of a salt hydrate (Tm hydrate), the melting of ice in presence of liquid and vapor (Tm ice) and the bulk homogenization to the liquid phase (Th (L); Table 4). No formation of liquid from the vola-

**Table 3c.** Chemical composition of opaque minerals

| Mineral | Awaruite | | Heazlewoodite | Pentlandite | | Chalcocite | "Native copper" | | |
|---|---|---|---|---|---|---|---|---|---|
| Sample | To(3) | Mg 159c | Mg 159c | To3 | To3 | SP | To3 | To3 | SP |
| Weight-% | | | | | | | | | |
| Fe | 24.46 | 25.01 | 0.28 | 39.52 | 41.50 | 2.30 | 2.80 | 1.13 | 2.12 |
| Ni | 75.74 | 76.55 | 74.01 | 24.57 | 23.76 | 0.05 | 2.43 | 3.75 | 4.08 |
| Co | 0.49 | 0.34 | 0.40 | 2.02 | 0.60 | – | – | – | – |
| Cu | 0.00 | 0.00 | 0.00 | 0.00 | 0.00 | 77.73 | 94.84 | 94.20 | 93.40 |
| S | 0.00 | 0.02 | 27.24 | 33.48 | 33.31 | 20.68 | – | – | – |
| Total | 100.68 | 101.92 | 101.93 | 99.60 | 99.23 | 100.80 | 100.09 | 99.09 | 99.60 |
| Atomic-% | | | | | | | | | |
| Fe | 25.22 | 25.48 | 0.01 | 5.44 | 5.72 | 0.07 | 2.95 | 1.20 | 2.25 |
| Ni | 74.30 | 74.16 | 2.97 | 3.20 | 3.12 | 0.00 | 2.43 | 3.79 | 4.10 |
| Co | 0.48 | 0.33 | 0.03 | 0.28 | 0.08 | – | – | – | – |
| Cu | 0.00 | 0.00 | 0.00 | 0.00 | 0.00 | 1.90 | 94.60 | 94.99 | 93.66 |
| S | 0.00 | 0.00 | 2.00 | 8.00 | 8.00 | 1.00 | – | – | – |

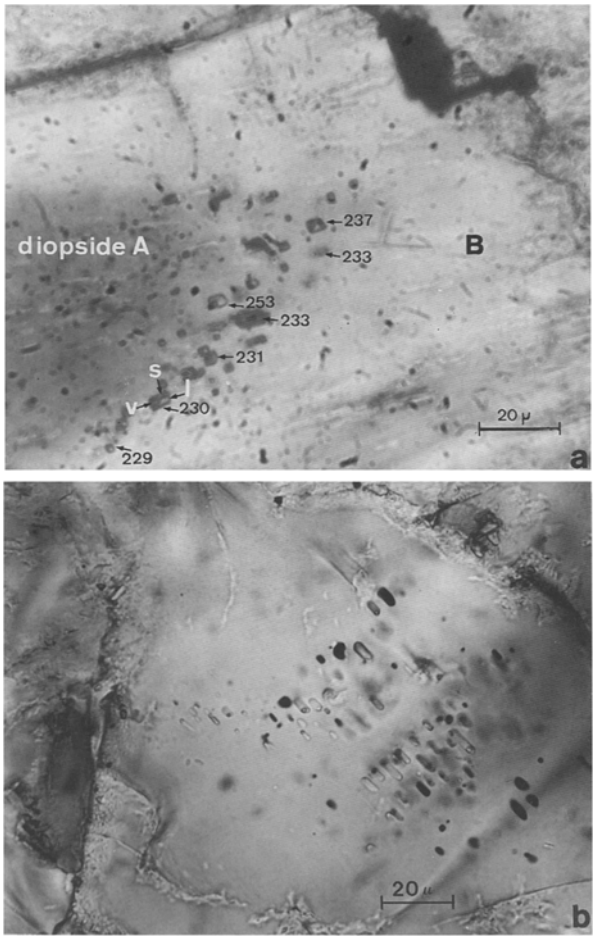


**Fig. 10. a** Microphotograph of primary aqueous fluid inclusions L1 occurring in the contact zone between *diopsides A* and *B*. Homogenization temperatures indicated; **b** microphotograph of pseudosecondary aqueous fluid inclusions L2 occurring in diopside B

**Table 4.** Microthermometric data (all temperatures in °C)

| S Nr. | Incl. type | Te | $Tm_{hydrate}$ | $Tm_{ice}$ | Th (L) | V (%) | D |
|---|---|---|---|---|---|---|---|
| To3.2 | L1 | | | | 229 | | 3 |
| To3.2 | L1 | −42 | | −6.8 | 230 | | 4 |
| To3.2 | L1 | | | | 231 | | 3 |
| To3.2 | L1 | −46 | −24.5 | −6.9 | 253 | | 4 |
| To3.2 | L1 | | | | 233 | | 5 |
| To3.2 | L1 | | | | 233 | | 4 |
| To3.2 | L1 | | | −6.8 | 237 | | 4 |
| To3.1 | L1 | | | −6.7 | | | 5 |
| To3.1 | L1 | −36 | | −6.9 | | | 6 |
| To3.1 | L1 | −45 | −24.0 | −7.2 | | | 10 |
| To3 | L2 | −36 | | −8.6 | 256 | 11 | 5 |
| To3 | L2 | −33 | | −7.8 | 222 | 19 | 6 |
| To3 | L2 | −32 | | −7.7 | 233 | 12 | 6 |
| To3 | L2 | | | −7.7 | 237 | 16 | 8 |
| To3 | L2 | | | −7.9 | 232 | | 7 |
| To3 | L2 | | | −8.3 | | | 6 |
| To3 | L2 | | | −8.1 | 230 | | 5 |
| To3 | L2 | | | −8.6 | 237 | | 6 |
| To3 | L2 | | | −8.6 | 228 | | 5 |
| To3 | L2 | | | | 219 | | 7 |
| To3 | L2 | | | | 230 | | 7 |
| To3 | L2 | | | | 225 | | 7 |
| To3 | L2 | | | | 254 | | 7 |
| To3 | L2 | | | | 234 | | 7 |
| To3 | L2 | | | | 235 | | 7 |
| To3 | L2 | | | | 231 | | 6 |

S Nr., sample number; Incl. type, inclusion type; Te, maximum temperature of first melting (eutectic); $Tm_{hydrate}$, hydrohalite melting temperature; $Tm_{ice}$, ice melting temperature; Th (L), homogenization temperature of vapor and liquid to the liquid state; V (%), volume-% of the vapor phase at room temperature deduced from microphotograph assuming a cylindrical inclusion shape; D, largest dimension of the inclusion in micrometers

tile phase nor of a gas clathrate occurred upon cooling. Th is similar for both types of inclusions and lies between 219 and 256° C. By contrast, primary L1 inclusions differ from early secondary L2 inclusions by lower Te values, the presence of a salt hydrate dissociating at −24° C and by slightly higher Tm ice. Because of the small size of the inclusions, the Tm ice values represent maximum temperatures. The inferred salinity is approximately 10.4 wt.% NaCl equivalents (Potter et al. 1978). Based on the eutectic (Te) and the salt hydrate dissociation temperatures (Tm hydrate), the L1 aqueous fluid can be interpreted in the $H_2O-NaCl-CaCl_2$ system containing 5.1 wt.% $CaCl_2$ and 6.4 wt.% NaCl (Yanatieva 1956). As no salt hydrate dissolution temperature was observed in L2 inclusions, probably because of the small size of the fluid inclusions, only a rough salinity of around 12 wt.% NaCl equivalents can be inferred without any information about the $Ca^{2+}/Na^+$ or $Mg^{2+}/Na^+$ ratios.

*Raman analyses*

Raman analyses were carried out with an X–Y Dilor multichannel Raman spectrometer using the 514.5 nm exciting radiation of an Ar ion laser (Type 2020, Spectra-Physics). The vapor bubble diameter of fluid inclusions L1 and L2 is usually around 1 µm. Two constraints made the gas analysis very difficult. First, the vapor phase was often moving outside the focused point of the laser beam. Second, the laser power had to be held at less than 1 watt to avoid heating the diopside and consequently destroying the fluid inclusion. One inclusion of type L1 was larger than the others with a vapor diameter around 2.5 µm. In this inclusion we succeeded in identifying molecular $H_2$ as shown in Fig. 11, but no $CO_2$, $CH_4$, $H_2S$, or $N_2$ were found. In L2 fluid inclusions, no volatiles were detected. However, it is not known whether the negative result was caused by the very difficult analytical conditions or if it indicates lower $H_2$ density. The spectral resolution of the spectrometer does not permit the shift of the vibrational band Q(1) to be monitored as a function of the vapor density. However, the relatively high quality of the spectrum for the very small size of the vapor phase suggests the $H_2$ molar volume to be in the range 100 to 1000 mole $cm^{-3}$. The $H_2$ concentration in L1 inclusions, calculated from the molar volume of the vapor phase and its volume fraction (0.15) is between 0.3 and 3 mol%.

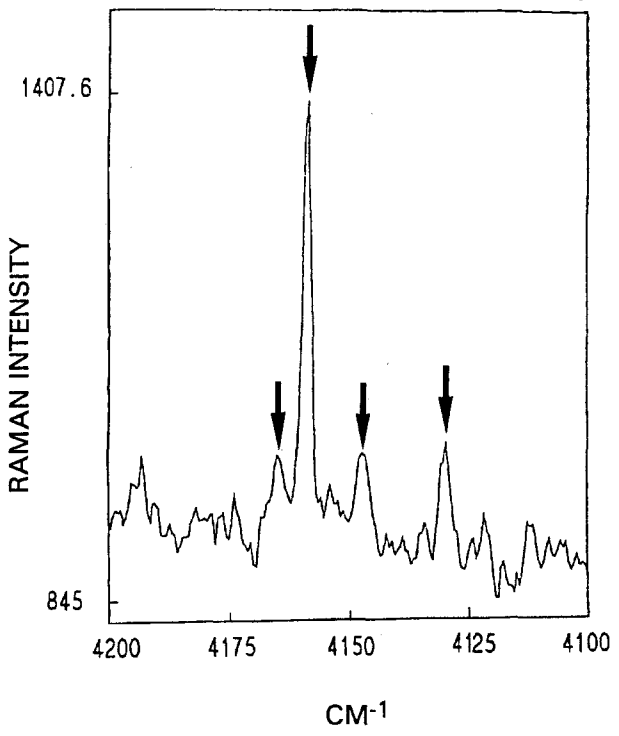


**Fig. 11.** Raman spectrum of $H_2$ from the vapor phase of a 10 μm large size fluid inclusion L1. Diameter of measured vapor bubble is 2.5 μm

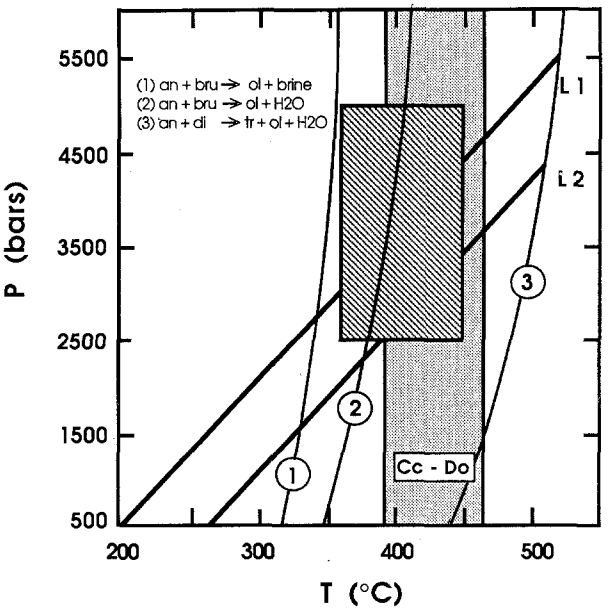


**Fig. 12.** Pressure-temperature constraints for the trapping conditions of fluid inclusions in the Malenco serpentinite. The activities of components in solid and fluid phases are given in the text. *Cc Do*, temperature estimation using calcite-dolomite thermometery (Mellini et al. 1987). *L1, L2*, isochores of the fluid inclusion populations L1 and L2. The *box* approximates possible trapping conditions of fluid inclusions containing hydrogen (stability field of antigorite-olivine-diopside). *An*, antigorite; *ol*, olivine; *bru*, brucite; *trem*, tremolite; *di*, diopside

## Thermodynamic calculations

### *Isochore calculation*

As the P–T–V–X properties of the $H_2O-H_2-CaCl_2-NaCl$ system are unknown, only isochores based on the properties of the $H_2O-CaCl_2-NaCl$ system can be constructed. Calculations were carried out using the experimental data and the model of Zhang and Frantz (1987). The effect of $H_2$ on the isochore can be estimated from Henry's constant for $H_2$, as derived from the solubility data of the literature regressed by Drummond (1981). The gas solubility in a complex electrolyte can be estimated from the solubility of the same gas in a 1-1 electrolyte of the same ionic strength (Franck 1985). The 5.4 wt.% $CaCl_2$ and 6.2 wt.% NaCl corresponds to a 2 molal NaCl aqueous solution. The Henry's constant ($K_H$) for the $H_2$ solubility, expressed in the molality scale ($m_{H_2}$), is 1000 at 200° C in a 2 molal NaCl solution. Therefore an $H_2$ concentration of 1 mol% implies a $H_2$ partial pressure of 500 bars according to the Henry's law equation $P(H_2)=K_H \cdot m_{H_2}$. Thus, the origin of the isochore at 200° C is expected to be shifted toward higher pressures by at least several hundreds of bars up to 1 kb (Fig. 12).

### *P–T–f(O₂)–f(S₂)-calculations*

The assemblage antigorite-brucite-olivine is used to formulate a dehydration reaction that univariantly relates P and T (Table 2). Because aqueous fluid inclusions were found in diopside its stability limit according to reaction (c) (Table 2) is of importance (Fig. 12).

The dehydration curves were calculated using the thermodynamic data base of Berman (1988) and the Perplex computer program (Connolly 1990). The component activities in the minerals were calculated from the $X_{Mg}$ values given in Table 3a, assuming ideal solid solutions which results in the following activities: $a_{fo}$ (olivine) = 0.90, $a_{bru}$ (brucite) = 0.93, $a_{an}$ (antigorite) = 0.97, $a_{dio}$ (diopside) = 0.96, $a_{tr}$ (tremolite) = 0.96 ($X_{Mg}$ of tremolite from Trommsdorff and Evans 1972). The activity of $H_2O$ has been determined as follows. The fluid inclusion analyses show that the fluid present during regional metamorphism was not pure but rather it was an aqueous solution in the system $H_2O-H_2-NaCl-CaCl_2$ or an even more complex system. The resulting decrease of the activity of water ($a_{H_2O}$),was calculated using the Bowers and Helgeson (1983) equation of state for $X_{NaCl}$ (equivalent) = 0.035, the salt concentration indicated by the microthermometric study of fluid inclusions (Table 4, Tm ice = −6.9° C, sample To3). It represents a first approximation for a fluid of a much more complicated composition. Because of the similar Alpine and tectonic events in the Margna and the Malenco nappe the pressures determinated in the Margna nappe are assumed to be a good approximation for the conditions in the Malenco nappe. The pressures reached during the different Alpine tectonic events were between 4–7 kb as estimated from barroisite occurrences in amphibolites of the Margna nappe (Guntli and Liniger 1989). Based on

calcite-dolomite geothermometry, Mellini et al. (1987) estimated the upper range of temperatures as 390–465° C. These P–T estimations are compatible with the stable occurrence of antigorite-olivine-diopside and the estimated trapping conditions of the fluid inclusions (Fig. 12). On the basis of these constraints on P and T, the $f(O_2)$ and $f(S_2)$ can be calculated using the opaque equilibria:

$$\underset{\text{heazlewoodite}}{Ni_3S_2} + 1/3 \underset{\text{magnetite}}{Fe_3O_4} = \underset{\text{awaruite}}{FeNi_3} + 4/6\,O_2 + S_2 \quad \text{(HAM)}$$

and

$$2\,Cu + 1/2\,S_2 = \underset{\text{chalcocite.}}{Cu_2S} \quad \text{(CuCc)}$$
copper

The thermodynamic data used for the calculation of the (HAM) equilibrium are compiled by Peretti and Connolly (in prep.) using data of Ono et al. (1977), Leech and Sykes (1939), Robie et al. (1979) and Ferrante and Gokcen (1982). The $f(O_2)$ can be determined by the (HAM) and (CuCc) equilibria. The $f(S_2)$ of the CuCc-buffer at elevated temperatures and pressures was calculated using the data from Bowers et al. (1984).

As is discussed in more detail by Peretti and Connolly the $\log f(O_2)$ is between $-30$ and $-31$ at $\log f(S_2) = -15.5$, $P = 3.5$ kb and $T = 400°$ C. At $\log f(S_2) = -15.8$, $P = 4.5$ kb and $T = 450°$ C, $\log f(O_2)$ is between $-29$ and $-30$. These $f(O_2)$ values indicate strongly reducing conditions, 4 log units below the QFM (quartz-fayalite-magnetite) buffer. As is indicated by Fig. 7, the $f(O_2)$ indicated by the presence of pentlandite-awaruite-magnetite is even lower than the $f(O_2)$ indicated by the presence of awaruite-heazlewoodite-magnetite, at any given P, T and $f(S_2)$.

## Discussion and conclusions

The regional mapping of metamorphic mineral assemblages in the Malenco serpentinite localizes the contemporaneous occurrence of the fluid inclusions with the assemblage diopside-antigorite-olivine-brucite as well as the opaque assemblage magnetite-native copper-chalcocite-pentlandite-heazlewoodite-awaruite. This mineral assemblage was used to constrain the P–T–X conditions of the metamorphic fluid and to compare it with the data derived from the fluid inclusions.

The metamorphic fluids are composed of saline aqueous solutions containing free hydrogen as documented by microthermometry and Raman spectroscopy. The presence of metal chlorides in the fluids coincides with the prediction by Eugster and Baumgartner (1987) on the basis of fluid rock interaction calculations of $H_2O$–HCl fluids with ultramafitites. The presence of $H_2$ can be interpreted as a result of internal control of oxygen fugacity and the occurrence of dehydration reactions without the introduction of external fluids (Frost 1985).

The assemblages pentlandite-awaruite-magnetite and copper-chalcocite indicate an $f(O_2)$ of at least 4 log units below the QFM buffer, favoring the presence of $H_2$ in aqueous solutions. This is due to the increase of the $f(H_2)/f(H_2O)$ ratio in aqueous fluids with decreasing $f(O_2)$ as can be deduced from the dissociation constant of water:

$$H_2O \Leftrightarrow H_2 + 1/2\,O_2$$

with $K_{diss}(P, T) = \{f(H_2) \cdot f(O_2)^{1/2}\}/f(H_2O)$

The mineral assemblage antigorite-olivine-brucite in the matrix of the analysed fluid inclusions was used to constrain the P–T conditions with the reaction:

$$\text{antigorite} + \text{brucite} \rightarrow \text{olivine} + H_2O,$$

which represents a univariant reaction in the P–T plane (Fig. 12, reaction 2). The trapping conditions inferred from the intersection of the isochore of the fluid with the univariant P–T dehydration reactions intersect roughly between 350 to 450° C and 2500 to 4500 bar (Fig. 12, box) representing greenschist facies metamorphic conditions. Under these metamorphic conditions, Frost (1985) predicted a corresponding $H_2$ concentration between 1 and 10 mol% at 4 log units below QFM, 375° C and 2 kb. The $H_2$ concentration determined from fluid inclusions are 0.3 to 3 mol%, partly covering the predicted range. However, whether the observed $H_2$-concentration is a reliable indicator of the redox state of the fluid at trapping conditions depends on the achievement of chemical equilibrium, on uncertainties in determination of $H_2$ concentrations as well as on its post-trapping equilibration ($H_2$ diffusion). The $H_2O$–$H_2$ redox pair is known to equilibrate rapidly with minerals down to 200° C as shown by Giggenbach (1987) in fluids of active geothermal systems. Therefore, disequilibrium during trapping can be ruled out. The main uncertainty in the $H_2$ concentration concerns the estimation of the molar volume of the vapor phase at room temperature. Therefore, a range of 0.3 to 3 mol% $H_2$ concentrations is mentioned to cover this source of uncertainty. The presence of hydrogen obviously demonstrates that diffusional loss was not complete.

Formation of hydrogen requires conditions that occur only in very special geological environments in the Earth's crust. Hydrogen has been found in $CH_4$–$C_2H_6$-bearing fluid inclusions in chkalovite from the Illimaussak alkaline intrusion (Greenland; Konnerup-Madsen et al. 1985). In quartz associated with uranium deposits (Dubessy et al. 1988) no $H_2$ was found but only reduced fluids containing $CH_4$. This is due to the presence of graphite in those rocks. Compared with other fluids of the continental crust, such a reduced fluid strongly contrasts with the redox state of fluids at equilibrium with carbon-bearing metasediments. Typical $fO_2$ values of such metamorphic fluids calculated by French (1966), Ohmoto and Kerrick (1979) or from fluid inclusion compositions (Dubessy et al. 1989) are between the QFM and Ni–NiO buffers. Therefore, the incorporation of periodites or serpentinites in the continental crust may favor the formation of highly reducing conditions either during serpentinization (Neal and Stanger 1983; Coveney et al. 1987) or by deserpentinization during prograde metamorphism as it is shown for the Malenco serpentinite.

*Acknowledgements.* A. Peretti was supported by the Schweizerischer National fond project no. 2.601-0.85 and no. 2.4728-0.87. He wishes to thank J. Connolly for thermodynamic calculations. The authors thank M. Cuney (CREGU) for helpful comments. L. Diamond is greatly acknowledged for his careful review which significantly clarified the manuscript.

## References

Arnorsson S (1985) Gas pressures in geothermal systems. Chem Geol 49:319–328

Barnes I, O'Neil JR (1969) The relationship between fluids in some fresh alpine-type unltramafics and some possible modern serpentinization, western United States. GSA Bull 80:1947–1960

Berman RG (1988) Internally consistent thermodynamic data for minerals in the system $Na_2O-K_2O-CaO-MgO-FeO-Fe_2O_3-SiO_2-TiO_2-H_2O-CO_2$. J Petrol 29:445–552

Bowers TS, Helgeson HC (1983) Calculation of the thermodynamic and geochemical consequences of non ideal mixing in the system $H_2O-CO_2-NaCl$ on phase relations in geological systems: equation of state for $H_2O-CO_2-NaCl$ fluids at high pressures and temperatures. Geochim Cosmochim Acta 47:1247–1275

Bowers TS, Jackson KJ, Helgeson HC (1984) Equilibrium activity diagrams for coexisting minerals and aqueous solutions at pressures and temperatures to 5 kbar and 600° C. Springer, Berlin Heidelberg New York Tokyo

Bucher K, Pfeifer HR (1973) Über Metamorphose und Deformation der östlichen Malenco-Ultramafitite und deren Rahmengesteine (Prov. Sondrio, N-Italien). Schweiz Mineral Petrogr Mitt 53:231–241

Connolly J (1990) Multivariable phase diagrams: an algorithim based on generalized thermodynamics. Am J Sci 290:666–718

Coveney RM Jr, Goebel ED, Zeller EJ, Dreschhoff GAM, Agino EE (1987) Serpentinization and the origin of hydrogen gas in Kansas. Am Ass Petroleum Geil Bull 71:39–48

De Capitani L, Ferrario A, Montrasio A (1981) Metallogeny of the Malenco metaophiolitic complex, Central Alps. Ofioliti 6:87–100

De Quervain F (1963) Die Erzmineralien von Selva-Quadrada (Puschlav). Schweiz Mineral Petrogr Mitt 43:295–314

Dietrich V (1969) Die Ophiolithe des Oberhalbsteins (Graubünden) und das Ophiolithmaterial der Ostschweizerischen Molasse. Ein petrographischer Vergleich. Eur Hochschulz XVII:1

Drummond SE (1981) Boiling and mixing of hydrothermal fluids: chemical effects on mineral precipitation. Unpublished Thesis, Penn State University, USA

Dubessy J (1984) Simulation des équilibres chimiques dans le système C–O–H. Conséquences méthodologiques pour les inclusions fluides. Bull Mineral 107:155–168

Dubessy J, Pagel M, Beny JM, Christensen H, Hickel B, Kosztolanyi, Poty B (1988) Radiolysis evidenced by $H_2-O_2$ and $H_2$-bearing fluid inclusions in three uranium deposits. Geochim Cosmochim Acta 52:1155–1167

Dubessy J, Poty B, Ramboz C (1989) Advances in C-O-H-N-S fluid geochemistry based on micro-Raman spectrometric analysis of fluid inclusions. Eur J Mineral 1:517–534

Eckstrand OR (1975) The Dumont serpentinite: a model for control of nickeliferous opaque mineral assemblages by alteration reactions in ultramafic rocks. Econ Geol 70:183–201

Ellis AJ (1979) Explored geothermal systems. In: Barnes HL (ed) Geochemistry of hydrothermal ore deposits, 2nd edn. Wiley, New York, pp 632–683

Eugster HP, Baumgartner L (1987) Mineral solubilities and speciation in supercritical metamorphic fluids. In: Carmichael ISE, Eugster HP (eds) Thermodynamic modelling of geological materials: minerals, fluids and melts. Rev Min 17:367–398

Evans BW, Trommsdorff V (1970) Regional metamorphism of ultramafic rocks in the Central Alps: parageneses in the system $CaO-MgO-SiO_2-H_2O$. Schweiz Mineral Petrogr Mitt 50:481–492

Evans BW, Trommsdorff V (1972) Der Einfluss der Eisens auf die Hydratisierung von Duniten. Schweiz Mineral Petrogr Mitt 52:251–256

Evans BW, Johannes W, Oterdoom H, Trommsdorff V (1976) Stability of chrysotile and antigorite in the serpentinite multisystem. Schweiz Mineral Petrogr Mitt 56:79–93

Ferrante MJ, Gokcen NA (1982) Relative enthalpies of $Ni_3S_2$. Bull Mines RI 8745:1–14

Ferrario A, Montrasio A (1976) Manganese ore deposit of Monte del Forno. Its stratigraphic and structural implications. Schweiz Mineral Petrogr Mitt 56:377–386

French BM (1966) Some geological implications of equilibrium between graphite and a C-H-O phase at high temperatures and pressures. Rev Geophys 4:223–253

Franck EU (1985) Aqueous mixtures to supercritical temperatures and at high pressures. Pure Appl Chem 57 (8):1065–1070

Frost BR (1985) On the stability of sulfides, oxides and native metals in serpentinite. J Petrol 26 (1):31–63

Giggenbach WF (1987) Redox processes governing the chemistry of fumarolic gas discharges from White Island, New Zealand. Appl Geochem 2:143–161

Guntli P, Liniger M (1989) Präalpine und alpine Metamorphose in Bereich des Piz de la Margna (Margna Decke). Schweiz Mineral Petrogr Mitt 69:289–301

Hall DL, Bodnar RJ (1990) Methane in fluid inclusions from granulites: a product of H2 diffusion? Geochim Cosmochim Acta 54:641–651

Hall DL, Bodnar RJ, Craig JR (1990) Fluid evolution during metamorphism and uplift of the massive sulfide deposits at Ducktown, Tennessee, USA II. Evidence for compositional changes to fluid inclusions via hydrogen diffusion. Am Mineral

Hollister LS, Burruss RC (1976) Phase equilibria in fluid inclusions from the Khtada Lake metamorphic complex. Geochim Cosmochim Acta 40:163–175

Konnerup-Madsen J, Dubessy J, Rose-Hansen J (1985) Combined raman microprobe and microthermometry of fluid inclusions in minerals from igneous rocks of the Gardar (South Greenland). Lithos 18:271–280

Kunze G (1961) Antigorit. Strukturchemische Grundlagen und ihre praktische Bedeutung für die weitere Serpentin-Forschung. Fortschr Mineral 39:206–324

Leech P, Sykes DS (1939) The evidence for a superlattice in the nickel-iron alloy $Ni_3Fe$. Phil Mag 7 (27):742–753

Liniger M, Guntli P (1988) Bau und Geschichte des zentralen Teils der Margna-Decke. Schweiz Mineral Petrogr Mitt 68:41–54

Montrasio A (1984) The "Lanzada Scermendone Zone": an ophiolitic unit of continental affinity in the southern Rhaetic Alps (Prov. Sondrio-Italy). Schweiz Mineral Petrogr Mitt 64:111–129

Mellini M, Trommsdorff V, Compagnoni R (1987) Antigorite polysomatism: behaviour during prograde metamorphism. Contr Mineral Petrol 97:147–155

Neal C, Stanger G (1983) Hydrogen generation from mantle source rocks in Oman. Earth Planet Sci Lett 66:315–320

Ohmoto H, Kerrick DM (1977) Devolatilization equilibria in graphitic systems. Am J Sci 277:1013–1044

Ono K, Ueda Y, Yamaguchi A, Moriyama J (1977) Themodynamic study of Fe–Ni solid solution. Trans Japan Inst Metals 18:610–616

Peretti A (1985) Der Monte del Forno Komplex am Bergell-Ostrand: Seine Lithostratigraphie, alpine Tektonik und Metamorphose. Ecolgae Geol Helv 78:23–48

Peretti A (1988) Occurrence and stabilities of opaque minerals in the Malenco serpentinite (Sondrio, Northern Italy). Unpublished PhD Thesis, ETH, Switzerland

Peters TI (1968) Distribution of Mg, Fe, Al, Ca and Na in coexisting olivine, orthopyroxene and clinopyroxene in the Totalp Serpentinite (Davos, Switzerland) and in the Alpine metamor-

phosed Malenco Serpentine (N-Italy). Contrib Mineral Petrol 18:65–75
Potter RW II, Clynne MA, Brown DL (1978) Freezing point depression of aqueous sodium solutions. Econ Geol 73:284–285
Poty B, Leroy J, Jachimowicz L (1976) Un nouvel appareil pour la mesure des températures sous le microscope: l'installation de microthermométrie Chaixmeca. Bull Soc Fr Mineral Crist 99:182–186
Robie RA, Hemingway BS, Fischer JR (1979) Thermodynamic properties of minerals and related substances at 298.15 K and 1 bar ($10^5$ pascals) pressure and at high temperatures. US Geol Surv Bull 1452
Staub R (1946) Geologische Karte der Berninagruppe 1:50000. Spez Karte Nr. 118. Schweiz Geol Kommission
Thayer TP (1966) Serpentinization considered as a constant volume metasomatic process. Am Mineral 51:685–710
Trommsdorff V, Evans BW (1972) Progressive metamorphism of antigorite shists in the Bergell tonalite aureole (Italy). Am J Sci 272:423–437
Trommsdorff V, Evans BW (1974) Alpine metamorphism of peridotitic rocks. Schweiz Mineral Petrogr Mitt 54:333–352
Trommsdorff V, Evans BW (1980) Titanian hydroxylclinohumite: Formation and breakdown in antigorite rocks (Malenco, Italy). Contrib Mineral Petrol 72:229–242
Trommsdorff V, Nievergelt P (1983) The Bregaglia (Bergell) lorio intrusive and its field relations. Mem Soc Geol It 26:55–68
Yanatieva OK (1946) Solubility polytherms in the system $CaCl_2-MgCl_2-H_2O$ and $CaCl_2-NaCl-H_2O$. Zh Prikl Khimii 19/7:707–722 (in Russian)
Zhang Y, Frantz JD (1987) Determination of the homogenization temperatures and densities of supercritical fluids in the system $NaCl-KCl-CaCl_2-H_2O$ using synthetic fluid inclusions. Chem Geol 64:335–350

Editorial responsibility: J. Hoefs